Nanoscale Res Lett (2009) 4:1035–1040
DOI 10.1007/s11671-009-9352-4

NANO EXPRESS

Facile Synthesis of Novel Nanostructured MnO_2 Thin Films and Their Application in Supercapacitors

H. Xia · W. Xiao · M. O. Lai · L. Lu

Received: 16 April 2009 / Accepted: 14 May 2009 / Published online: 2 June 2009

Abstract Nanostructured α-MnO_2 thin films with different morphologies are grown on the platinum substrates by a facile solution method without any assistance of template or surfactant. Microstructural characterization reveals that morphology evolution from dandelion-like spheres to nanoflakes of the as-grown MnO_2 is controlled by synthesis temperature. The capacitive behavior of the MnO_2 thin films with different morphologies are studied by cyclic voltammetry. The α-MnO_2 thin films composed of dandelion-like spheres exhibit high specific capacitance, good rate capability, and excellent long-term cycling stability.

Keywords Supercapacitor · MnO_2 · Nanostructure · Thin film · Cyclic voltammetry

Introduction

In recent years, manganese oxides (MnO_2) have attracted considerable interests due to their distinctive physical and chemical properties and wide applications in catalysis, ion exchange, molecular adsorption, biosensor, and energy storage [1–5]. Specifically, manganese oxides have been extensively evaluated as electrode materials for supercapacitors due to their low cost and environmental benignity compared to noble metal oxides such as RuO_2 [6–8]. In the development of supercapacitors, nanostructured electrode materials have received great interests as they exhibit higher specific capacitance and rate capability compared to traditional bulk materials. Over the years, various nanostructured manganese oxides, including one-dimensional (1-D) (nanorodes, nanowires, nanobelts, nanoneedles, and nanotubes), two-dimensional (2-D) (nanosheets, nanoflakes), and three-dimentional (3-D) (nanospheres, nanoflowers, hollow urchins) nanostructures, have been synthesized [9–16]. 3-D hierarchical porous structures often produce more active sites and exhibit more favorable electrochemical properties than 2-D and 1-D structures. However, facile synthesis and mass production of complex 3-D nanostructures are still a challenge in the areas of materials science [17–20]. It has been reported that a core-shell structure with spherically aligned nanorods of α-MnO_2 can be prepared through a simple room temperature reaction between $MnSO_4$ and $(NH_4)_2S_2O_8$ with a catalyst of Ag^+ in an acid solution [21]. A similar method used by Gong et al. is able to synthesize MnO_2 hollow urchins with a reactive template of carbon spheres [22]. Wang et al. also reported the synthesis of hierarchical α-MnO_2 spheres by the reaction between $MnSO_4$ and $K_2S_2O_8$ with the addition of $CuSO_4$ in an acidic solution [23]. However, the preparation of 3-D nanostructured MnO_2 in the thin film form has never been reported. Since the use of composite electrodes introduces additional undesirable interfaces in the electrode material with the risk of negating the benefits of electrochemistry using nanostructures, thin film electrodes enable us to investigate the electrochemical properties of the active material itself without the influence of binders and conductive additives as required for composite electrodes.

In this paper, we propose the stratagem to synthesize 3-D α-MnO_2 dandelion-like spheres and 2-D α-MnO_2 nanoflakes by a reaction between $MnSO_4$ and $(NH_4)_2S_2O_8$ in a Na_2SO_4 solution at low temperatures. With a platinum (Pt) substrate submerged into the reaction solution, the nanostructured MnO_2 can be directly deposited on the Pt

H. Xia · W. Xiao · M. O. Lai · L. Lu (✉)
Department of Mechanical Engineering, National University of Singapore, 9 Engineering Drive 1, Singapore 117576, Singapore
e-mail: luli@nus.edu.sg

substrate in the thin film form. The effects of the synthesis temperature on the morphology of the films are investigated, and the capacitive behaviors of nanostructured MnO_2 thin films with different morphologies are studied and compared.

Experimental

Synthesis of Nanostructured MnO_2

Analytical grade $MnSO_4$, $(NH_4)_2S_2O_8$, and Na_2SO_4 from Sigma–Aldrich were used. A typical synthesis of nanostructured MnO_2 was performed by dissolving $MnSO_4$, $(NH_4)_2S_2O_8$, and Na_2SO_4 with a molar ratio of 1:1:1 in 30 mL deionized water at room temperature. The concentrations of Mn^{2+}, $S_2O_8{}^{2-}$, and $SO_4{}^{2-}$ in the solution are the same as 0.1 mol L^{-1}. A Pt substrate was submerged into the solution, while the solution was magnetically stirred in a beaker at room temperature (RT) for 12 h or at 80 °C for 2 h. One side of the Pt substrate was covered with Parafilm, so that MnO_2 can only be deposited on one side. After the reaction, the Pt substrate was washed using distilled water and then dried in the vacuum at 60 °C overnight.

Characterization

Structure and crystallinity of thin films were characterized using a Shimadzu XRD-6000 X-ray diffractometer with Cu Kα radiation at a scanning rate of 1°min^{-1}. Surface morphology of the as-deposited thin films was characterized using a Hitachi S-4100 field emission scanning electron microscope (FESEM). Weights of the MnO_2 thin films were measured using a microbalance with an accuracy of 0.01 mg.

All electrochemical measurements were conducted using a Solartron 1287 electrochemical interface combined with a Solatron 1260 frequency response analyzer. For the electrochemical measurements, a three-electrode cell system composed of a MnO_2 thin film electrode as the working electrode, a high surface carbon rod as the counter electrode, and an Ag/AgCl reference electrode was employed. The capacitive behaviors of the as-deposited MnO_2 thin films were characterized by cyclic voltammetry (CV) in 1 M Na_2SO_4 electrolyte at room temperature. CV measurements were performed on the three-electrode cells in the voltage window between 0 and 0.9 V at different scan rates from 20 to 200 mV s^{-1}. Electrochemical impedance spectra (EIS) of different thin film electrodes were measured at the open-circuit potential in the frequency range from 100 kHz to 10 mHz.

Results and Discussion

Figure 1a, b shows the XRD patterns of the MnO_2 thin films synthesized at different temperatures. Notably, major diffraction peaks in Fig. 1a, b can be indexed as a tetragonal symmetry of α-MnO_2 with a space group of I4/m (JCPDS Card, No. 44-0141). Comparing Fig. 1a with Fig. 1b, it can be seen that the diffraction peaks in Fig. 1a are sharper and stronger, indicating that the degree of crystallinity of the products is enhanced as the synthesis temperature increases. However, some small impurity peaks observed from both Fig. 1a, b can be indexed as Mn_3O_4, which is probably due to the incomplete oxidation reaction between Mn^{2+} and $S_2O_8{}^{2-}$. The complete formation of MnO_2 from the solution can be expressed as the following reaction:

$$MnSO_4 + (NH_4)_2S_2O_8 + 2H_2O \rightarrow MnO_2 + (NH_4)_2SO_4 + 2H_2SO_4 \quad (1)$$

α-MnO_2 has usually been found to be the product of the oxidation of Mn^{2+} by $S_2O_8{}^{2-}$ either through a hydrothermal reaction [24] or through a mild solution reaction [21–23]. It has been observed in this study that the formation of nanostructured MnO_2 is preferred to deposit on the Pt substrate rather than in the solution. Therefore, the preparation of MnO_2 thin films (as shown in Fig. 1c) in this study is quite simple and convenient compared with electrochemical deposition, which is usually employed to prepare MnO_2 thin films.

The morphologies of the MnO_2 thin films synthesized at different temperatures are shown in Fig. 2. It can be seen from Fig. 2a that the film synthesized at RT is composed of uniform microscopic spheres with diameters ranging from 0.5 to 1 μm. The magnified FESEM image (Fig. 2b) shows that these microscopic spheres are composed of

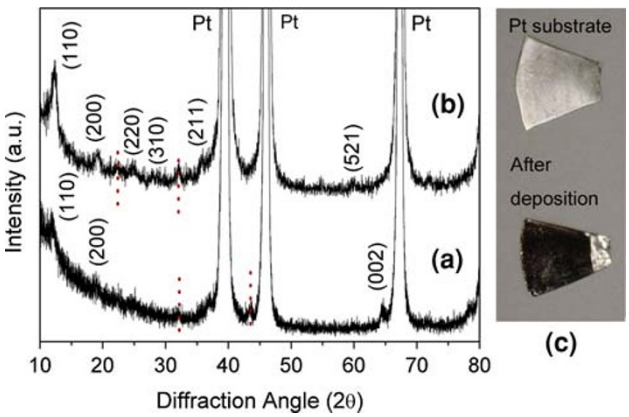

Fig. 1 **a** XRD pattern of the MnO_2 thin film synthesized at RT, **b** XRD pattern of the MnO_2 thin film synthesized at 80 °C (The *dotted lines* in *red* color represent the diffraction peaks from Mn_3O_4), and **c** photos of the Pt substrate before and after the deposition

nanowhiskers, resulting in a dandelion-like morphology. Li et al. [22] reported that a core-shell structure microspheres (2–3 μm) of α-MnO_2 can be obtained by the reaction between $MnSO_4$ and $(NH_4)_2S_2O_8$ with the addition of $AgNO_3$ catalyst at RT for 1–2 days. The thin shell of this structure is composed of nanorods, and this morphology can only be obtained with the existence of Ag^+. Wang et al. [23] reported that sea urchin-shaped microspheres (∼1 μm) of α-MnO_2 can be obtained by the reaction between $MnSO_4$ and $K_2S_2O_8$ with the addition of $CuSO_4$ at 70 °C for 3 days. In the present work, the 3-D hierarchical structure of α-MnO_2 can be obtained at RT in a relatively short synthesis time (12 h) without using any $AgNO_3$ or $CuSO_4$ since the addition of catalyst of $AgNO_3$ or $CuSO_4$ may induce Ag^+ or Cu^{2+} impurities in the final MnO_2 products [23]. It is assumed that reaction between Mn^{2+} and $S_2O_8^{2-}$ in the Na_2SO_4 solution with a Pt substrate is relatively faster compared to the previous studies [22, 23]. It is interesting to observe a morphology evolution of the film, as the synthesis temperature increases. As shown in Fig. 2d, the film synthesized at 80 °C exhibits another type of porous structure with nanoflakes almost vertically aligned on the Pt substrate. The magnified FESEM image (Fig. 2e) shows that the average size of the nanoflakes is about 500 nm, and the thickness of the nanoflakes is less than 50 nm.

The possible formation mechanism for the hierarchical MnO_2 spheres is schematically illustrated in Fig. 2c. Generally speaking, the crystal growth process always includes two steps: the initial nucleation stage and following crystal growth stage [25, 26]. Initially, MnO_2 colloids are slowly formed and attached to the Pt substrate. After which, the absorbed MnO_2 colloids on the Pt substrate tend to aggregate loosely to form spherical appearance due to their high surface energies. Because the reaction temperature is at RT, Gibbs energy for nucleation of new MnO_2 sites is low. As a consequence, MnO_2 colloids tend to attach on the habit planes of existing MnO_2 sites, leading to the formation of 1-D nanowhiskers from the initial colloidal microspheres. With increase in the processing duration, finally dandelion-like 3-D microspheres of MnO_2 on the Pt substrate appear. However, on the contrary to Wang's finding [23], the increase in reaction temperature in this study is unable to improve the formation of 3-D hierarchical microspheres of MnO_2 but leads to the formation of 2-D nanoflakes. This phenomenon can be explained by the change in growth mechanisms as shown in Fig. 2f. When the reaction temperature is

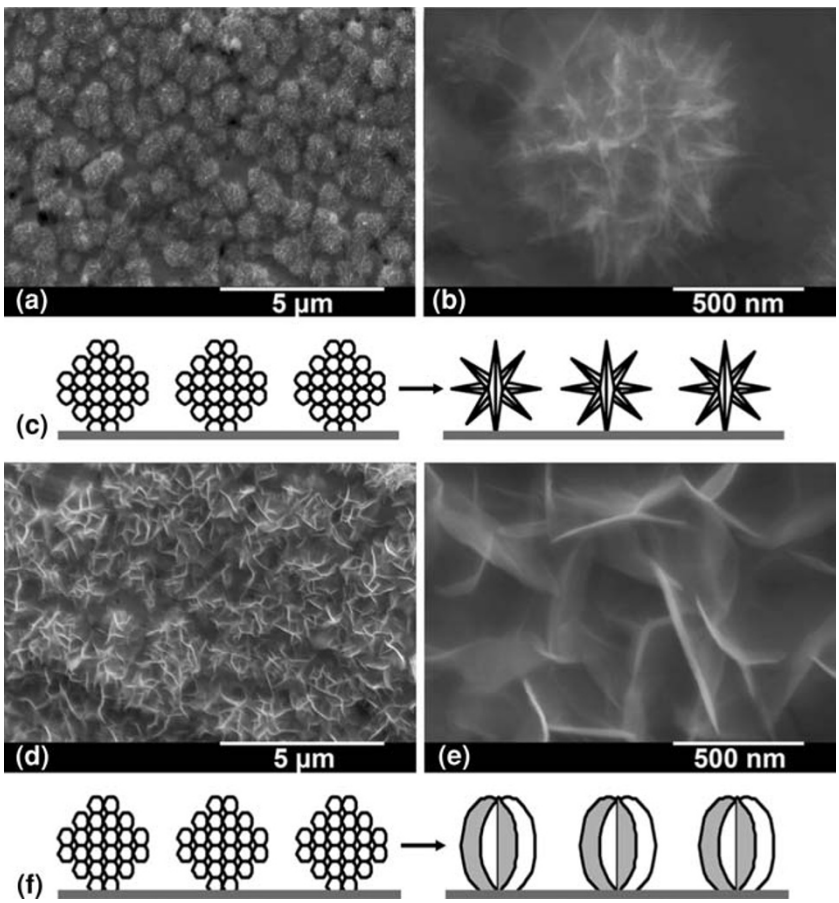

Fig. 2 FESEM images for RT synthesized MnO_2: **a** low magnification and **b** high magnification, **c** schematic illustration for the possible formation mechanism of dandelion-like MnO_2 microspheres, FESEM images for 80 °C synthesized MnO_2: **d** low magnification and **e** high magnification, and **f** schematic illustration for the possible formation mechanism of MnO_2 nanoflakes

increased to 80 °C, the reaction rate is greatly enhanced along with the high rate of adsorption of MnO_2 colloids to the Pt substrate. Under such circumstances, in addition to the one-dimentional growth of the nuclei along the low energy direction [27], the growth of the nuclei along other directions can also happen due to the fast nucleation and adsorption rates of MnO_2 at an elevated temperature. Therefore, nanoflakes instead of nanowhiskers form resulting in the morphology evolution.

The 3-D and 2-D nanostructured MnO_2 are promising as electrode materials for supercapacitors due to their porous structure, large surface area, and short diffusion length for protons or alkali cations. In order to evaluate the electrochemical properties of the as-deposited thin films, the thin film samples with different nanostructures were characterized in aqueous 0.1 M Na_2SO_4 electrolyte with CV measurements. The CV curves at various scan rates from 20 to 200 mV s^{-1} for the sample A and B are shown in Fig. 3a, b (sample A represents MnO_2 with dandelion-like sphere morphology, and sample B represents MnO_2 nanoflakes). It can be seen that the curves at the low scan rate of 20 mV s^{-1} for both samples exhibit ideal symmetrical rectangle-like shape indicating ideal capacitive behavior. As the scan rate increases, slight distortion from the ideal symmetrical rectangle shape can be observed from the CV curves for both samples. However, it is clear to see that the distortion from the rectangularity of the CV curves for the sample A is much less than that for the sample B, indicating much better rate performance of the sample A due to its finer nano-architecture. The specific capacitance of the nanostructured MnO_2 film can be obtained by the following equation:

$$C(F/g) = \frac{Q}{\Delta E \cdot m} \tag{2}$$

where Q is the voltammetric charge, ΔE is the voltage window (0.9 V), and m is the mass of the active material of the electrode. The specific capacitances at different scan rates for both samples are shown in Fig. 3c. At the scan rate 20 mV s^{-1}, the sample A exhibits a much higher specific capacitance of about 230 F/g than 180 F/g of the sample B. As the scan rate increases, the specific capacitance for both samples decreases, which is typical for electrochemically active MnO_2 materials. At the highest scan rate of 200 mV s^{-1}, the sample A can maintain 66% of its full capacitance (we set the specific capacitance at 20 mV s^{-1} as the full capacitance) while the sample B can only maintain 55% of its full capacitance, indicating that the sample A has much better rate capability than that of the sample B. Figure 3d compares the Nyquist plots for the MnO_2 thin films with different nanostructures. A depressed semicircle in the high-frequency range corresponding to the charge-transfer resistance, and a straight sloping line in the low-frequency range corresponding to the diffusive resistance can be observed for both samples. As shown in Fig. 3d, it is clear that the sample A has lower charge-

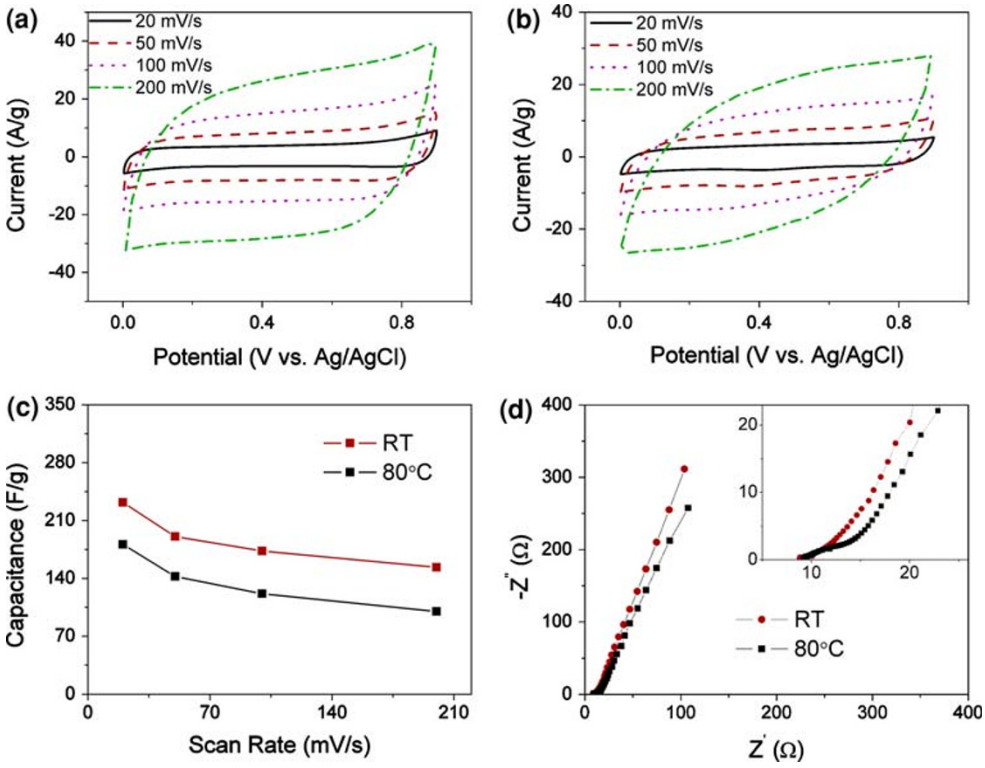

Fig. 3 **a** The CV curves at various scan rates from 20 to 200 mV s^{-1} for the MnO_2 film synthesized at RT, **b** the CV curves at various scan rates from 20 to 200 mV s^{-1} for the MnO_2 film synthesized at 80 °C, **c** specific capacitance at various scan rates for the MnO_2 thin films with different nanostructures, and **d** EIS spectra of MnO_2 thin films with different nanostructures

transfer resistance and diffusive resistance compared with those of the sample B, confirming the superior capacitive behavior of the sample A. Based on the previous paper by Chou et al. [28], surface area of thin film can be derived from the double layer capacitance by fitting EIS using equivalent circuit. The calculated surface areas of the sample A and the sample B are about 414 and 125 $m^2\ g^{-1}$ respectively. Pseudocapacitance of MnO_2 mainly originates from the adsorption of cations in the electrolyte ($M^+ = Li^+$, Na^+, and K^+) on the surface of MnO_2 and also possible intercalation/deintercalation of H^+ and alkaline metal cations in the bulk of MnO_2 [29]. Since the 3-D dandelion-like microspheres of the sample A are composed of much finer nanowhiskers with very small size, they provide a much larger surface area per gram and shorter diffusion length for cations, comparing to the relatively large 2-D nanoflakes of the sample B. Therefore, the morphology advantage of sample A explains why it can exhibit a higher specific capacitance and better rate capability than those of the sample B.

The sample A, showing better capacitive behavior in rate capability test, was further investigated for long-term cycling stability. The CV curves at different cycling stages and variation of specific capacitance over 2,000 cycles are shown in Fig. 4a, b. As shown in Fig. 4a, the CV curves for the 1st, 500th, 1000th, and 2000th cycles almost overlapped with each other, indicating excellent cycling stability. After 2,000 cycles, there is no degradation of the capacitive behavior, indicating no significant structural or microstructural changes in the MnO_2 thin film electrodes. The CV curve after 2,000 cycles is noted to become more symmetrical with the rectangular shape compared with the first cycle, indicating improved capacitive behavior after long time cycling. The specific capacitance of the sample A (as shown in Fig. 4b) slightly decreases for the first 30–40 cycles then starts to increase very slowly with the cycling. As shown in the XRD results, there is a small amount of Mn_3O_4 exist in the film. Mn with a lower oxidation state in the Mn_3O_4 is probably oxidized to Mn^{4+} during the long time CV cycling, resulting in improved capacitive behavior and an small increase of specific capacitance.

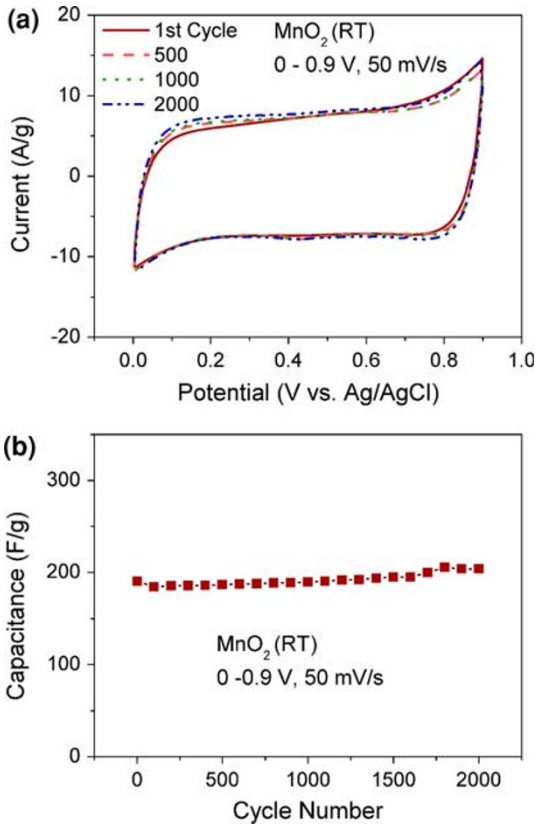

Fig. 4 **a** CV curves for the 1st, 500th, 1,000th, and 2,000th cycles for the MnO_2 thin film synthesized at RT and **b** the variation of specific capacitance with respect to cycle number for the MnO_2 thin film synthesized at RT

Conclusions

MnO_2 thin films with nanostructures have been prepared on Pt substrates by a facile and mild solution method. The MnO_2 film prepared at RT with a long reaction time is composed of dandelion-like microspheres, which consists of nanowhiskers with very small size. The reaction temperature plays an important role in controlling the surface morphology of the film. As the reaction temperature was increased to 80 °C, a film composed of nanoflakes can be prepared in a very short time. The CV measurements indicate that MnO_2 thin films prepared by this method are promising as electrodes for supercapacitors. The film composed of dandelion-like microspheres exhibited a higher specific capacitance and better rate capability than the film composed of nanoflakes, which is probably due to the high surface area and smaller feature of the microspheres. The excellent cycling stability and good rate capability of the film composed of dandelion-like microspheres coupled with the simple and low cost synthesis method make this material attractive for large applications.

Acknowledgments This research is supported by National University of Singapore and Agency for Science, Technology and Research through the research grant R-265-000-292-305 (072 134 0051).

References

1. Y.S. Ding, X.F. Shen, S. Sithambaram, S. Gomez, R. Kumar, V.M.B. Crisostomo, S.L. Suib, M. Aindow, Chem. Mater. **17**, 5382 (2005). doi:10.1021/cm051294w

2. O. Giraldo, S.L. Brock, W.S. Willis, M. Marquez, S.L. Suib, S. Ching, J. Am. Chem. Soc. **122**, 9330 (2000). doi:10.1021/ja001860i
3. Y.S. Ding, X.F. Shen, S. Gomez, H. Luo, M. Aindow, S.L. Suib, Adv. Funct. Mater. **16**, 549 (2006). doi:10.1002/adfm.200500436
4. J. Yu, T. Zhao, B. Zeng, Electrochem. Commun. **10**, 1318 (2008). doi:10.1016/j.elecom.2008.06.028
5. V. Subramanian, H.W. Zhu, B.Q. Wei, Electrochem. Commun. **8**, 827 (2006). doi:10.1016/j.elecom.2006.02.027
6. S.L. Chou, J.Z. Wang, S.Y. Chew, H.K. Liu, S.X. Dou, Electrochem. Commun. **10**, 1724 (2008). doi:10.1016/j.elecom.2008.08.051
7. K.R. Prasad, N. Miura, Electrochem. Commun. **6**, 1004 (2004). doi:10.1016/j.elecom.2004.07.017
8. M.S. Wu, P.C.J. Chiang, Electrochem. Commun. **8**, 383 (2006). doi:10.1016/j.elecom.2005.12.014
9. H. Xia, W. Xiao, M.O. Lai, L. Lu, Funct. Mater. Lett. **2**, 13 (2009). doi:10.1142/S1793604709000478
10. X. Wang, Y.D. Li, J. Am. Chem. Soc. **124**, 2880 (2002). doi:10.1021/ja0177105
11. M.S. Wu, J.T. Lee, Y.Y. Wang, C.C. Wan, J. Phys. Chem. B. **108**, 16331 (2004). doi:10.1021/jp0404955
12. F.Y. Cheng, J.Z. Zhao, W.N. Song, C.S. Li, H. Ma, J. Chen, P.W. Shen, Inorg. Chem. **45**, 2038 (2006). doi:10.1021/ic051715b
13. R.Z. Ma, Y. Bando, L.Q. Zhang, T. Sasaki, Adv. Mater. **16**, 918 (2004). doi:10.1002/adma.200306592
14. N. Wang, Y. Gao, J. Gong, X.Y. Ma, X.L. Zhang, Y.H. Guo, L.Y. Qu, Eur. J. Inorg. Chem. **2008,** 3827 (2008). doi:10.1002/ejic.200800236
15. M.W. Xu, L.B. Kong, W.J. Zhou, H.L. Li, J. Phys. Chem. C. **111**, 19141 (2007). doi:10.1021/jp076730b
16. J.P. Ni, W.C. Lu, L.M. Zhang, B.H. Yue, X.F. Shang, Y. Lv, J. Phys. Chem. C. **113**, 54 (2009). doi:10.1021/jp806454r
17. C.L. Yan, D.F. Xue, J. Phys. Chem. B. **110**, 1581 (2006). doi:10.1021/jp056373+
18. C.L. Yan, D.F. Xue, Adv. Mater. **20**, 1055 (2008). doi:10.1002/adma.200701752
19. J. Liu, D.F. Xue, Adv. Mater. **20**, 2622 (2008). doi:10.1002/adma.200800208
20. X. Zhao, X. Ren, C.T. Sun, X. Zhang, Y.F. Si, C.G. Yan, J.S. Xu, D.F. Xue, Funct. Mater. Lett. **1**, 167 (2008). doi:10.1142/S1793604708000393
21. Z.Q. Li, Y. Ding, Y.J. Xiong, Q. Yang, Y. Xie, Chem. Commun. (Camb) 918 (2005). doi:10.1039/b414204g
22. B.X. Li, G.X. Rong, Y. Xie, L.F. Huang, C.Q. Feng, Inorg. Chem. **45**, 6404 (2006). doi:10.1021/ic0606274
23. H.E. Wang, Z.G. Lu, D. Qian, S.P. Fang, J.F. Zhang, J. Alloys Compd. **466**, 250 (2008). doi:10.1016/j.jallcom.2007.11.041
24. V. Subramanian, H.W. Zhu, R. Vajtai, P.M. Ajayan, B.Q. Wei, J. Phys. Chem. B. **109**, 20207 (2005). doi:10.1021/jp0543330
25. J.S. Xu, D.F. Xue, Y.C. Zhu, J. Phys. Chem. B. **110**, 17400 (2006). doi:10.1021/jp0632788
26. L. Lu, L.P. Li, X.J. Wang, G.S. Li, J. Phys. Chem. B. **109**, 17151 (2005). doi:10.1021/jp052780+
27. C.C. Hu, K.H. Chang, Y.T. Wu, C.Y. Hung, C.C. Lin, Y.T. Tsai, Electrochem. Commun. **10**, 1792 (2008). doi:10.1016/j.elecom.2008.09.011
28. S.L. Chou, F.Y. Chen, J. Chen, J. Power Sources **162**, 727 (2006). doi:10.1016/j.jpowsour.2006.06.033
29. W.F. Wei, X.W. Cui, W.X. Chen, D.G. Ivey, J. Phys. Chem. C. **112**, 15075 (2008). doi:10.1021/jp804044s